Available online at www.sciencedirect.com
ScienceDirect
Trans. Nonferrous Met. Soc. China 33(2023) 3583−3596
Transactions of Nonferrous Metals Society of China
www.tnmsc.cn

Microstructure and properties of Al−Si functionally graded materials for electronic packaging

Wei ZHOU[1], Ri-chu WANG[1,2], Chao-qun PENG[1], Zhi-yong CAI[1,2]

1. School of Materials Science and Engineering, Central South University, Changsha 410083, China;
2. Key Laboratory of Electronic Packaging and Advanced Functional Materials, Central South University, Changsha 410083, China

Received 22 June 2022; accepted 9 November 2022

Abstract: Two- and three-layer Al−Si functionally graded materials (FGMs) for electronic packaging were prepared by spray deposition. The results show that dense microstructure and good interlayer bonding are obtained in the FGMs. The flexural strength of the three-layer FGMs is higher than that of the two-layer FGMs, and the flexural strength in the H−L direction with high Si content layer as the bearing surface is higher than that in the L−H direction with low Si content layer as the bearing surface. The thermal conductivity of all the FGMs exceeds 140 W/(m·K), and the coefficient of thermal expansion (CTE) shows no significant difference. After thermal shock treatment, more and larger cracks are found in the two-layer FGM than in the three-layer FGMs. This phenomenon is due to the high thermal stress at the interfaces and the tendency of large Si particles to rupture as a result of stress concentration.

Key words: electronic packaging; functionally graded material; Al−Si alloy; finite element analysis; thermal shock resistance

1 Introduction

The rapid development of electronic technology has led to the evolution of microwave circuits and electronic components toward high power, miniaturization and complexity, and the resulting thermal management issues present a challenge to the field of electronic packaging [1]. Therefore, the development of high-performance electronic packaging materials is of great importance to the electronics industry. In general, ideal electronic packaging materials require low coefficient of thermal expansion (CTE) and high thermal conductivity, while maintaining good mechanical properties, processability and laser weldability [2−5].

Hypereutectic Al−Si alloys (12%−70%) have been widely used in aerospace and electronics as electronic packaging materials due to their excellent properties, such as low density, high thermal conductivity, and low CTE [6−9]. The CTE of Al−Si alloys can be tailored by adjusting the content of Si. For those Al−Si alloys with high Si content, conventional casting methods usually lead to the presence of coarse and brittle Si phase, resulting in significant degradation in mechanical properties and processability [10,11]. Therefore, several methods have been developed to refine the microstructure, including spray deposition [12,13], pressure infiltration [14], selective laser melting [15], semi-solid squeezing [7], and rapid solidification/powder metallurgy (RS/PM) [6]. Among them, spray deposition is considered as an effective technique with high productivity, low oxidation and near-net products [16,17].

Studies have been carried out on the preparation of Al−Si alloys for improving the

Corresponding author: Zhi-yong CAI, Tel: +86-15575900596, E-mail: zycaimse@163.com
DOI: 10.1016/S1003-6326(23)66356-3

performance [18−20]. However, the researches mainly focus on the mechanical and thermo-physical properties of Al−Si alloys, while ignoring their processability and laser weldability. When the Si content is higher than 50%, Al−Si alloys acquire a low CTE but become hard and brittle [21]. The excessive Si phases make machining and welding highly difficult, resulting in poor gas tightness and increased costs. When the Si content is low, Al−Si alloys possess high thermal conductivity and are more suitable for surface plating or laser welding, but their CTE hardly meets the requirements [22]. The contradiction between CTE and processability is unlikely to be solved by improving preparation methods.

Functionally graded materials (FGMs) offer a promising solution to this problem. FGMs are multiphase systems in which the composition varies spatially to obtain unusual combinations of the mechanical, thermal or electrical properties [23,24]. In this way, the respective advantages of high Si content and low Si content Al−Si alloys can be well combined. The layers with high Si content are suitable for chip integration, while the layers with low Si content are suitable for machining and welding. Consequently, Al−Si FGMs can simultaneously meet the requirements of electronic packaging for low CTE, high thermal conductivity, and excellent processability and laser weldability. ZHOU et al [25] prepared a gradient packaging shell made of hypereutectic Al−Si alloy using liquid−solid separation technology, stating its performance meets the need for different parts. HUO et al [26] used laser melting deposition technology to prepare a gradient Al−Si alloy that was proved to be qualified for use in an aerospace environment. Although a few studies have been conducted, these have failed to systematically investigate the effects of layer number and composition on the performance of Al−Si FGMs.

In the present work, two- and three-layer Al−Si FGMs were prepared by spray deposition. Their microstructure, mechanical and thermo-physical properties were investigated. Considering that the FGMs may undergo severe cyclic heating/cooling during service, their thermal shock resistance was examined by thermal shock treatment. Finite element analysis was employed to calculate the stress distribution under mechanical and thermal loads.

2 Experimental

2.1 Materials preparation

According to the requirements of electronic packaging, the Si content distribution in an ideal packaging shell is shown in Fig. 1(a). In the present work, the Al−22wt.%Si and Al−70wt.%Si alloys were selected as the top layer for sealing and the bottom layer for chip integration, respectively. The two alloys were combined to form a two-layer FGM. To moderate the gradient, Al−42wt.%Si alloy or Al−50wt.%Si alloy was designed as a transition layer in the two-layer FGM to form three-layer FGMs, as shown in Fig. 1(b). In summary, three types of Al−Si FGMs were designed, namely Al−22/70Si, Al−22/42/70Si and Al−22/50/70Si FGMs. The gradient structures of these FGMs are listed in Table 1.

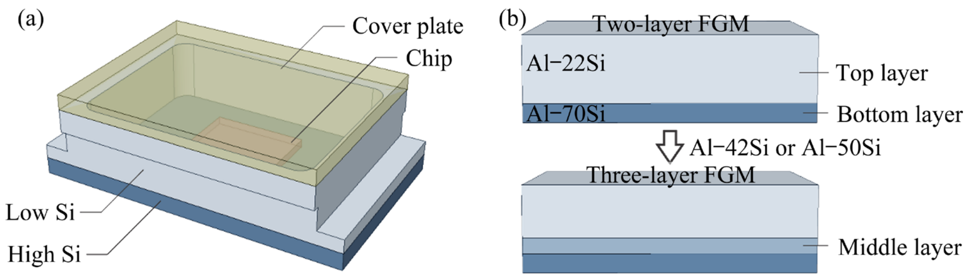

Fig. 1 Schematic diagrams of Si content distribution in ideal packaging shell (a), and two- and three-layer FGMs (b)

Table 1 Gradient structures of Al−Si FGMs for electronic packaging

Number	Alloy composition/wt.%			Layer thickness/mm		
	Top layer	Middle layer	Bottom layer	Top layer	Middle layer	Bottom layer
1	Al−22Si	−	Al−70Si	5	−	5
2	Al−22Si	Al−42Si	Al−70Si	5	1	4
3	Al−22Si	Al−50Si	Al−70Si	5	1	4

Based on the designed gradient structures, the two- and three-layer Al−Si FGMs were prepared by spray deposition. The raw materials including pure Al (99.9%) and polycrystalline pure Si (99.9%) were prepared according to the mass fraction and melted in an induction melting furnace, and then the molten metal was poured into the preheated crucible of the spray deposition equipment. After the first layer of the alloy was deposited using nitrogen as the atomization gas, the deposited surface was machined to obtain the desired thickness of the layer. The post-sintering density of each layer was taken into account to control the thickness. Subsequently, the second layer of alloy was deposited on the machined surface of the first layer, and the previous steps were repeated until the desired number of layers was obtained. Finally, the green billet was hot pressed in a graphite die at 550 °C and 120 MPa with a holding time of 240 min. For subsequent characterization and testing, three-layer FGMs with a transition layer thickness of 5 mm were prepared by the same method.

2.2 Characterization and testing

The microstructure of the Al−Si FGMs was observed under a field-emission scanning electron microscope (SEM, FEI Quanta 200). Samples for microstructure observation were prepared by grinding on SiC abrasive papers and then polishing with a 1 μm-diamond paste, followed by etching with Keller's reagent (1% HF + 1.5% HCl + 2.5% HNO_3 + 95% H_2O, in volume fraction) for 20 s. Each constituent layer was examined using an energy dispersive spectrometer (EDS, EDAX Genesis), as well as an X-ray diffractometer (XRD, Rigaku D/Max 2500) in a 2θ range of 20°−80°, with a scanning rate of 2 (°)/min. The density of the constituent layers and the FGMs was determined by the Archimedes method.

The Brinell hardness of the constituent layers of the Al−Si FGMs was determined using a hardness tester (HBS−3000B) under a load of 9.8 N for 30 s, and the Vickers hardness across the layers was determined using a microhardness meter (Buehler 5140) under a load of 9.8 N for 15 s. At least, three measurements were taken for each case. The flexural strength of the constituent layers of the FGMs were measured. Samples of 3 mm × 10 mm × 50 mm were prepared for the three-point bending test, and tested on a servo-hydraulic materials testing system (MTS 858) with a span of 30 mm. The effective flexural strength of the FGMs was measured using multilayer samples with each layer being close to the same thickness. There are two placement directions for the multilayer samples as shown in Fig. 2, including the L−H (low Si−high Si) direction with low Si content layer as the bearing surface, and the H−L (high Si−low Si) direction with high Si content layer as the bearing surface. The flexural strength of the samples (σ) was calculated by

$$\sigma=\frac{3PL}{2bh^2} \tag{1}$$

where P is the load, L is the span, and b and h are the width and thickness of the sample, respectively. Three nominally identical samples were used in each case to obtain the average value of the flexural strength.

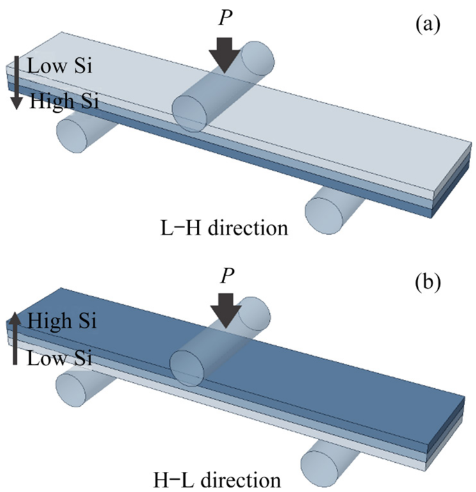

Fig. 2 Schematic diagrams of three-point bending test in L−H direction (a) and H−L direction (b)

The thermo-physical properties of the constituent layers of the Al−Si FGMs were measured. Samples of d12.6 mm × 3 mm were ground and polished, and subsequently measured on a thermal diffusivity analyzer (NETZSCH LFA 427) at room temperature. The thermal diffusivity and the specific heat were evaluated using the laser flash method at room temperature. The thermal conductivity of the samples (λ) was thus calculated by

$$\lambda=\rho\alpha C_p \tag{2}$$

where ρ is the density, α is the thermal diffusivity, and C_p is the specific heat capacity. The results were averaged over three measurements. The dilatometric measurements were performed in an argon atmosphere from 25 to 300 °C at a heating rate of 5 °C/min on a dilatometer (NETZSCH DIL 402C), using bar samples of 5 mm × 5 mm × 25 mm. In addition, multilayer samples were used in the thermal diffusivity measurements to determine the effect of the interface on thermal conductivity, as well as the dilatometric measurements in the direction shown in Fig. 3.

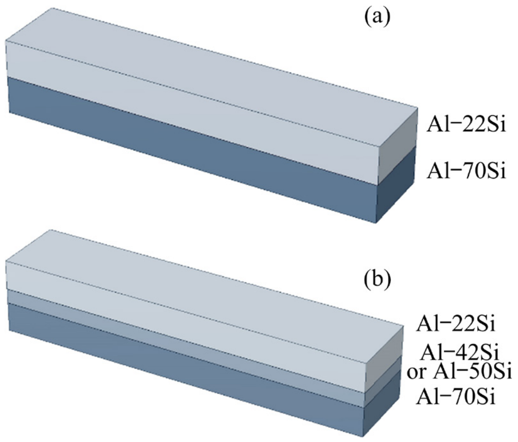

Fig. 3 Schematic diagram of two- (a) and three-layer (b) samples for CTE measurements

Thermal shock treatment was carried out to investigate the thermal shock resistance of the Al−Si FGMs. The dimensions of the samples were 3 mm × 10 mm × 10 mm, with the same thickness of each layer. During thermal shock treatment, the samples were heated in air inside a furnace to 300 °C, immersed for 10 min and then cooled in water at 25 °C for 2 min. The treatment was repeated up to 100 times under continuous heating and cooling, after which the microstructure of the FGMs was studied.

2.3 Finite element analysis

Three-dimensional finite element models were constructed based on the dimensions of the samples in the three-point bending test and thermal shock treatment, respectively, and then solved using the ANSYS software. It was assumed that the layers were all isotropic and well bonded. In the case of mechanical loading, a force of 300 N was applied to the center of the FGM beam, with a 30 mm span support, as shown in Fig. 2. In the case of thermal loading, the ambient temperature was set to cycle from 25 to 300 °C, as in the thermal shock treatment. Table 2 lists some basic properties of the constituents in the Al−Si FGMs, including density (ρ), elastic modulus (E), Poisson's ratio (μ), specific heat capacity (C_p), thermal conductivity (λ), and CTE (α).

3 Results and discussion

3.1 Microstructure

Figure 4 shows the back-scattered electron images of the Al−Si FGMs. The Al matrix appears dark and the Si phase appears light. As shown in Fig. 4, crack-free Al−Si FGMs with no apparent defects are obtained under the experimental conditions. The interface between the Al−22Si and Al−70Si layers is shown approximately as a straight line in Fig. 4(a), which is beneficial to the subsequent machining. As a result of spray deposition and hot pressing, a smooth transition from one layer to the other is observed at higher magnification in Fig. 4(b), with no obvious separation lines. There are two parts in Figs. 4(c) and (d) divided by the white lines, with the Al−22Si/Al−42Si (briefly 22/42) and Al−22Si/Al−50Si (22/50) interfaces on the left, and the Al−42Si/Al−70Si (42/70) and Al−50Si/Al−70Si (50/70) interfaces on the right. The interfaces in the Al−22/42/70Si and Al−22/50/70Si FGMs show similar features to the 22/70 interface, with a smoother transition due to the close Si content of their adjacent layers. It can be concluded from the microstructure of Al–Si FGMs that good interlayer bonding is obtained.

As shown in Fig. 4, the evolution of microstructure of each layer is mainly seen as the changes of the Si phase morphology, leading to the performance difference in different spatial locations. The inherent rapid cooling rate of spray deposition

Table 2 Material properties of constituents in Al−Si FGMs [27,28]

Constituent	ρ/(g·cm^{-3})	E/GPa	μ	C_p/(J·g^{-1}·K^{-1})	λ/(W·m^{-1}·K^{-1})	α/10^{-6}K^{-1}
Al	2.70	70	0.33	0.90	221	23.6
Si	2.33	113	0.22	0.70	135	4.1

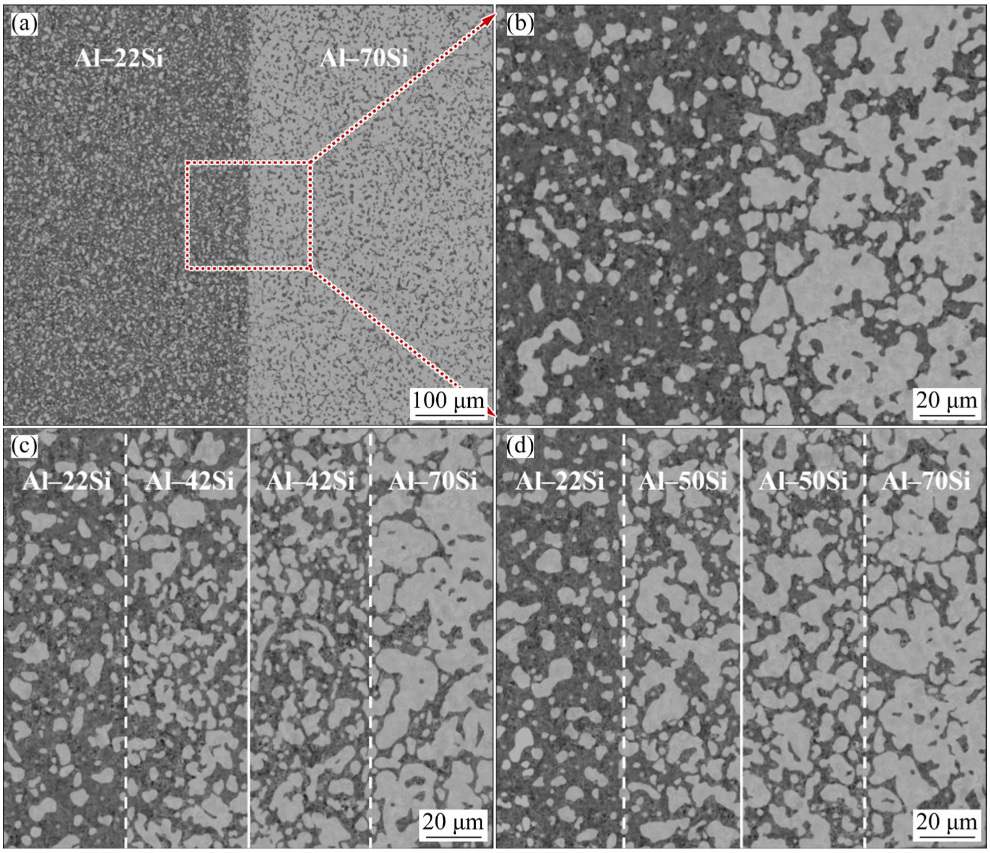

Fig. 4 Microstructures of Al−22/70Si (a, b), Al−22/42/70Si (c), and Al−22/50/70Si (d) FGMs

results in refined microstructures of the FGMs. Although the Si content of each layer is different, the Si phase is uniformly distributed in the Al matrix. When the Si content is low, the Si particles are fine and disperse in the matrix, which is beneficial to plating and welding, and maintain high thermal conductivity of the FGMs. As the Si content increases, the Si phase gradually increases while the Al matrix remains continuous. When the Si content is higher than 50%, the particle agglomeration becomes prevalent. The Si phase gradually develops an interconnected network-like structure, which helps to reduce the CTE.

Figure 5 shows the EDS spectra and element distribution maps of the Al−Si FGMs. The layers of the same composition in different FGMs show similar EDS profiles, one of which is selected for demonstration. It is seen that no impurity elements are detected. Since the scattering effect of impurity elements on electrons can cause hindrance to electrical and thermal conduction, this facilitates the acquisition of excellent physical properties such as high thermal conductivity of the FGMs [29]. All the layers maintain the designed composition in general, indicating that the composition distribution of the FGMs can be well controlled by adopting the layer-by-layer preparation method.

Figure 6 shows the XRD patterns of the constituent layers of the Al–Si FGMs. The XRD patterns of the layers with the same composition are similar in different FGMs. It is seen that all the diffraction peaks in the patterns belong to Al and Si. With the increase of Si content in the layers, the intensity of the Si diffraction peaks increases, while that of the Al diffraction peaks decreases. No additional intermetallic compounds or interfacial reaction products are found, indicating that the phases of each layer remain consistent during the preparation of the FGMs, or the amount of new phase is extremely small and undetectable.

The theoretical densities of the constituent layers and the Al−Si FGMs are calculated by the rule of mixtures using the densities of the constituents, and the relative densities are the ratio of the measured densities to the theoretical densities. The results are listed in Table 3. All the samples possess high relative densities, indicating that densification has been achieved through hot-pressing.

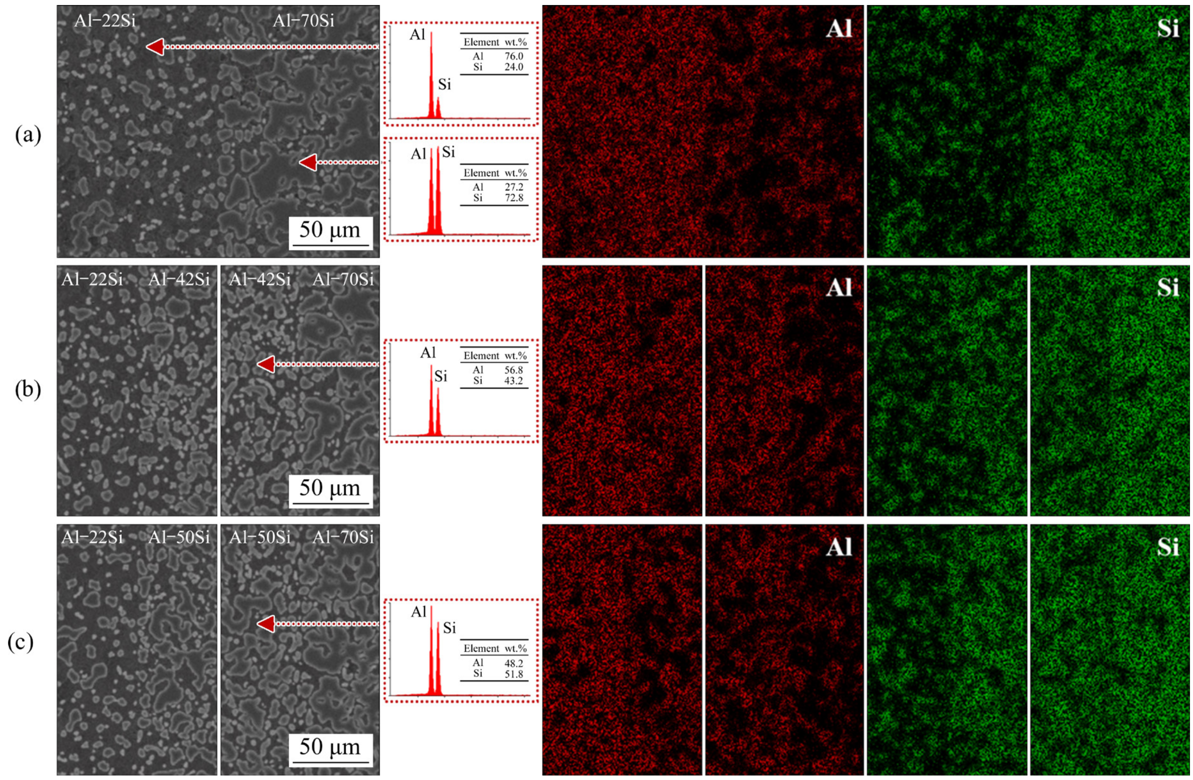

Fig. 5 EDS spectra and element distribution maps of Al−22/70Si (a), Al−22/42/70Si (b), and Al−22/50/70Si (c) FGMs

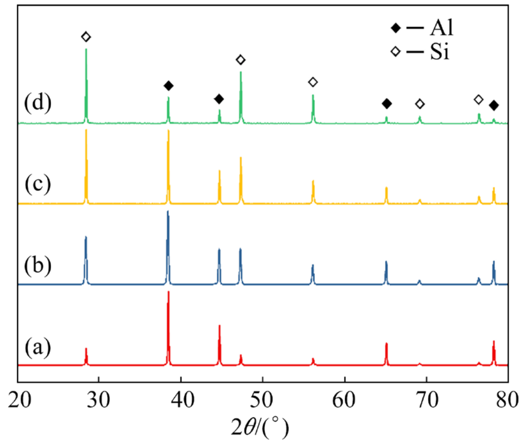

Fig. 6 XRD patterns of Al−22Si (a), Al−42Si (b), Al−50Si (c), and Al−70Si (d) layers

This will contribute to maintaining high strength and thermal conductivity, as these properties are largely influenced by density. The densities of the constituent layers are slightly higher than those of the FGMs. In multilayer materials, the interfaces with discontinuity in composition are usually a source of additional pore formation [30]. Therefore, compared with the layers, the FGMs exhibit lower relative densities. In addition, the relative density of three-layer FGMs is expected to be lower than that of the two-layer FGM. However, it is observed that the relative densities of the FGMs increase marginally with increasing the number of layers. This phenomenon is ascribed to the fact that the properties of two adjacent layers become closer to each other to allow better bonding between the layers.

Table 3 Densities of constituent layers and Al−Si FGMs

Sample	Experimental density/ ($g\cdot cm^{-3}$)	Theoretical density/ ($g\cdot cm^{-3}$)	Relative density/%
Al−22Si	2.608	2.619	99.6
Al−42Si	2.531	2.545	99.4
Al−50Si	2.503	2.515	99.5
Al−70Si	2.428	2.441	99.5
Al−22/70Si	2.497	2.530	98.7
Al−22/42/70Si	2.515	2.535	99.2
Al−22/50/70Si	2.502	2.525	99.1

3.2 Mechanical properties

Figure 7 shows the Brinell and Vickers hardness distribution on the cross section of the Al−Si FGMs, from top to bottom along the thickness direction. The Brinell and Vickers hardnesses of the FGMs increase with the increase of the hard Si phase in the constituent layer, i.e., with increasing Si content. The Brinell hardness within each layer remains almost consistent, indicating the uniform distribution of the Si phase in the Al matrix observed in the SEM images. The two-layer FGM exhibits a greater variation in Vickers hardness than the three-layer FGMs. The Vickers hardness values at the interfaces are between those of the adjacent layers on both sides, close to their average value.

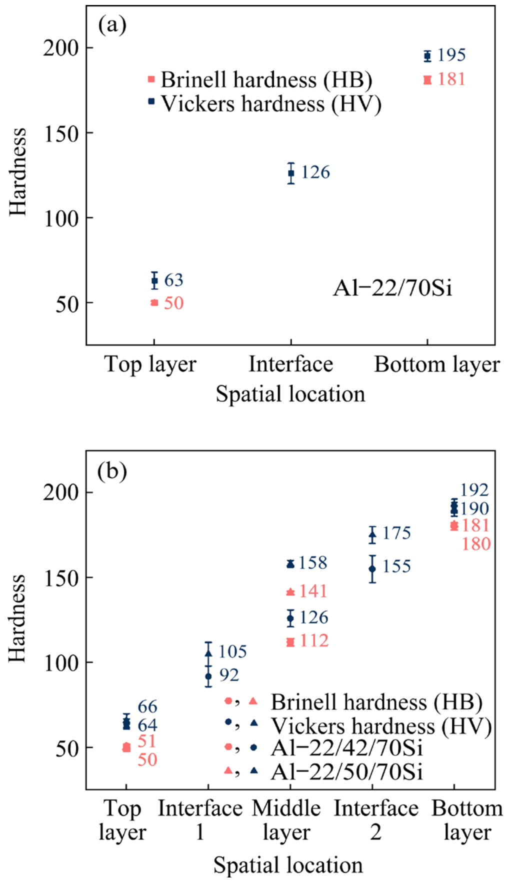

Fig. 7 Brinell and Vickers hardness distribution on cross-section of Al−22/70Si (a), and Al−22/42/70Si and Al−22/50/70Si (b) FGMs

Table 4 shows the mechanical properties of the constituent layers of the Al−Si FGMs. With the increase of Si content, the flexural strength of the alloys first increases and then decreases. Among them, the Al−42Si alloy has the highest flexural strength of 313 MPa. When the Si content is low, the dispersed Si phase in the Al matrix can effectively impede crack expansion, thus strengthening the alloy. However, when the Si content reaches above 50%, the strengthening effect of the brittle Si phase is substantially reduced. Most of the load is carried by the Si particles that break when the load exceeds their fracture strength, leading to premature failure of the material [31]. Therefore, the alloys with 42% and 50% Si achieve relatively high flexural strength. The elastic modulus of the alloys increases with increasing the Si content.

Table 4 Mechanical properties of constituent layers of Al−Si FGMs

Sample	Flexural strength/MPa	Elastic modulus/GPa
Al−22Si	258±8	78±3
Al−42Si	313±5	94±2
Al−50Si	303±4	102±1
Al−70Si	214±9	117±2

Table 5 shows the mechanical properties of the Al−Si FGMs, and Fig. 8 shows the bending stress−strain curves of the constituent layers and Al−Si FGMs. Compared with the two-layer FGM, the flexural strength of the three-layer FGMs is improved by at least 12% in both directions. Despite the difference in transition layer composition, the difference in flexural strength between the two types of three-layer FGMs is slight. For the same FGM, its flexural strength in the L−H direction is significantly lower than that in the H−L direction, while the elastic modulus shows no significant difference in both directions. As seen in Fig. 8(b), the bending stress−strain curves of the samples in the L−H and H−L directions are highly similar, while the former breaks sooner than the latter. Compared with the flexural strength of the constituent layers, the flexural strength of the FGMs in the L−H direction is lower than that of any of the constituent layers, while the flexural strength of the FGMs in the H−L direction is higher than that of any of the constituent layers.

Table 5 Mechanical properties of Al−Si FGMs

Sample	Flexural strength/MPa		*E*/GPa
	L−H	H−L	
Al−22/70Si	121±7	283±5	98±1
Al−22/42/70Si	139±4	326±8	96±1
Al−22/50/70Si	136±6	330±6	99±2

According to the ultimate loads in the three-point bending tests, the axial stress (σ_x) of the Al−Si FGMs under a load of 300 N is calculated using finite element analysis. The stress distribution in the central cross-section of the FGMs is shown in Fig. 9. The differences of axial stresses in all the FGMs are small with the same placement direction. In the L−H direction, the maximum axial stresses in the three-layer FGMs are even slightly increased compared with the two-layer FGM. This seems to be contrary to the experimental result that the flexural strength of the three-layer FGMs is higher than that of the two-layer FGM. An important factor may be the residual stress generated during the preparation process. High residual stresses lead to microcracks yielded ahead of macrocracks by weakening the interface between Al and Si grains, which is detrimental to the mechanical properties of the FGMs [30,32]. By introducing the transition layer, the residual stresses are reduced in the FGMs after cooling and the bonding between the layers is strengthened, which outweigh the adverse effects of the increased axial stresses. As a result, the flexural strength of the FGMs increases as the number of layers increases.

Comparing Figs. 9(b) and (c), it is seen that the stress distribution of the Al−22/42/70Si and Al−22/50/70Si FGMs is similar under the same load. There are only negligible differences in the maximum axial stresses in both the L−H and H−L directions for these two FGMs, and the Al−42Si and Al−50Si layers are actually of comparable flexural strengths, which are 313 and 303 MPa, respectively. Therefore, as the experimental results shown, the effect of transition layer composition on the flexural strength of the three-layer FGMs is small. In other words, the addition of transition layers of both

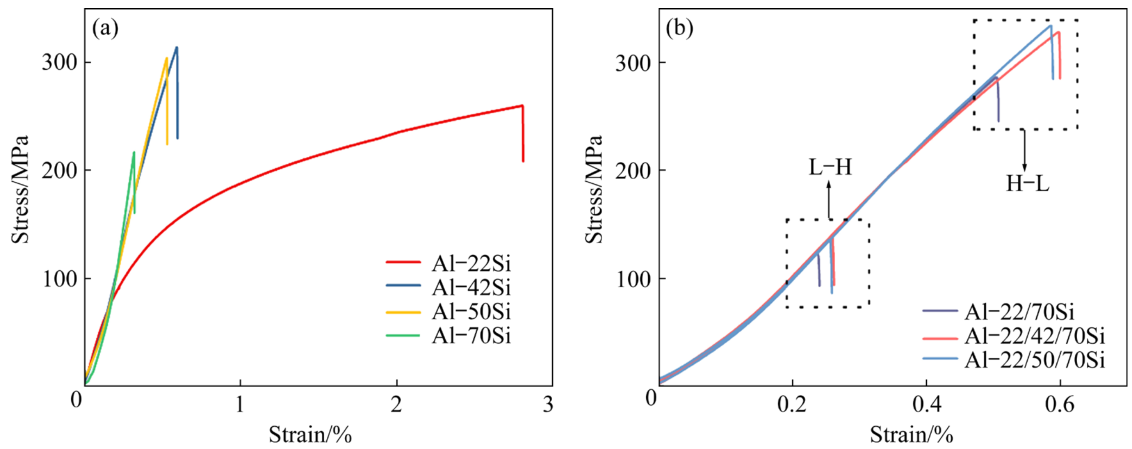

Fig. 8 Bending stress−strain curves of constituent layers (a) and Al−Si (b) FGMs

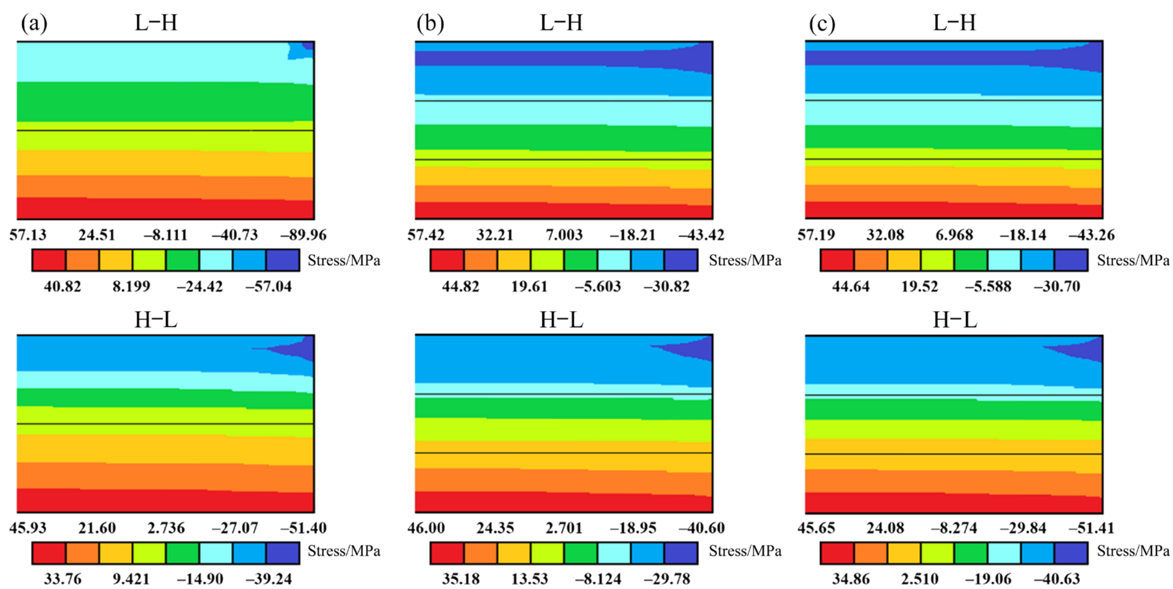

Fig. 9 Stress distribution in central cross-section of Al−22/70Si (a), Al−22/42/70Si (b), and Al−22/50/70Si (c) FGMs under load of 300 N

compositions is effective in reducing residual stresses and improving interlayer bonding.

In addition, the placement direction has a significant effect on the axial stress. In the H−L direction, the maximum axial stress of the FGMs is approximately 46 MPa, which is about 20% lower than that in the L−H direction (57 MPa). Both the two- and three-layer samples reach the maximum stress at the bottom surface, implying that cracks are most likely to initiate in this plane. Therefore, the load-bearing capacity of the samples depends more on the properties of the bottom surface. For the layers with different Si contents, their behavior in the three-point bending test is different. The layers with low Si content contribute to the resistance to tensile stress due to their ductility, while the layers with high Si content are hard enough to resist the compressive stress and provide a certain bending moment tolerance for the FGMs [33]. When the low Si content layer is loaded under tensile conditions, the FGMs are prone to crack formation and fracture. In contrast, when the high Si content layer is loaded under such conditions, the FGMs are able to bear more load before fracture. Consequently, the flexural strength of the FGMs in the H−L direction with the Al−22Si layer as the bottom surface is higher than that in the L−H direction with the Al−70Si layer as the bottom surface.

3.3 Thermo-physical properties

Table 6 shows the thermo-physical properties of the constituent layers of the Al−Si FGMs. As expected, the thermal conductivity of the samples decreases with the increase of Si content, and their CTE (from room temperature to 100, 200 and 300 °C, respectively) decreases as well. In the Al–Si FGMs, the CTE of the bottom layer reaches 8.7×10^{-6} K^{-1}, matching well with chip materials; the CTE of the top layer is 18.9×10^{-6} K^{-1}, close to that of the cover plate. Compared with other methods such as liquid−solid separation [25], the Al−Si alloys prepared by spray deposition have higher thermal conductivity at the same CTE. The CTE of all the layers exhibits a trend of increase with increasing temperature, which is determined by the microstructure of each layer. When the temperature increases, the Si network in the high Si content layer exerts a stronger constraining effect on the Al matrix, resulting in a lower CTE than the low Si content layer. However, the presence of more Si phases affects the heat transfer in the Al matrix. This is due to the reduced thermal conductivity of Si compared with Al, as well as the interfacial thermal resistance generated between the Si phase and the Al matrix.

Table 6 Thermo-physical properties of constituent layers of Al−Si FGMs

Sample	λ/(W·m^{-1}·K^{-1})	CTE/10^{-6} K^{-1}		
		100 °C	200 °C	300 °C
Al−22Si	180±2	16.2	17.9	18.9
Al−42Si	153±1	11.4	12.8	13.6
Al−50Si	142±2	9.8	11.0	11.7
Al−70Si	115±1	7.5	8.2	8.7

Table 7 lists the thermo-physical properties of the Al−Si FGMs, including the thermal conductivity, the CTE from room temperature to 100, 200 and 300 °C, respectively and the CTE mismatch between adjacent layers at 300 °C. The CTE of the three FGMs shows no significant difference. As expected, the CTE of the two-layer FGM is between that of the two constituent layers. Compared with the Al−22/70Si FGM, the CTE of the Al−22/42/70Si FGM is slightly increased, while that of the Al−22/50/70Si FGM is slightly decreased. Damage to multilayer materials exposed to thermal shock usually occurs in the form of delamination, cracking and bending deformation,

Table 7 Thermo-physical properties of Al−Si FGMs

Sample	λ/(W·m^{-1}·K^{-1})	CTE/10^{-6}K^{-1}			CTE mismatch at 300 °C/%	
		100 °C	200 °C	300 °C	δ_1	δ_2
Al−22/70Si	143±3	11.0	12.1	12.8	117	−
Al−22/42/70Si	153±4	11.1	12.3	13.0	40	56
Al−22/50/70Si	146±3	10.8	11.9	12.6	62	34

$\delta_k=(\alpha_k-\alpha_{k+1})/\alpha_{k+1}$, where α_k is the CTE of the kth layer from top and thermal stress is the main cause of these problems [1]. As the difference in CTE inevitably leads to thermal stress, electronic packaging materials require a CTE that matches the chip [34]. Provided that the Al−70Si layer can meet this requirement, the compatibility between adjacent layers of the FGMs needs to be considered. The different compositions of each layer lead to different degrees of CTE mismatch. Compared with the two-layer FGM, the CTE mismatch of the three-layer FGMs is substantially reduced. Therefore, increasing the number of layer is beneficial to reducing the thermal stress of the FGMs.

As listed in Table 7, all the FGMs achieve high thermal conductivity exceeding 140 W/(m·K). Compared with the two-layer FGM, the thermal conductivity of the three-layer FGMs shows no decrease with the addition of the transition layer. This indicates that the FGMs have good interlayer bonding, and there is no noticeable adverse effect with more interfaces on the thermal conductivity of the FGMs. Since the thermal conductivity of the Al−50Si alloy is higher than that of the Al−42Si alloy, the thermal conductivity of the Al−22/50/70Si FGM is higher than that of the Al−22/42/70Si FGM. Therefore, the thermal conductivity of the FGMs is highly related to that of the constituent layers.

3.4 Thermal shock resistance

Figure 10 shows the secondary electron images of the Al−Si FGMs after thermal shock treatment. No visible macroscopic cracks are observed in any of the three FGMs after 100 thermal shocks. However, the generation of coarse continuous cracks is observed near the interface of the two-layer FGM, while only fine cracks near the interface with high Si content are observed in the three-layer FGMs, i.e., the 42/70 and 50/70 interfaces. The cracks appear mainly in the continuous Si phase, hence more cracks in the constituent layers with high Si content. For the two-layer FGM, the cracks appear mostly in the Al−70Si layer; for the three-layer FGMs, the cracks appear in both the transition layers and the Al−70Si layer. This phenomenon is ascribed to the fact that the Si particles of large size are prone to stress concentration and rupture [35]. Within each layer, the microstructures show no significant changes, while the Si phase at the interface shows signs of fragmentation.

The crack length near the interface of the Al−Si FGMs is measured by avoiding the edge cracks at both ends of the samples. In the vicinity of the interface within 100 μm, the crack length per unit thickness in the cross-section of the FGMs is shown in Fig. 11. The one with the largest crack length among these FGMs is the Al−22/70Si FGM, and the one with the smallest length is the Al−22/50/70Si FGM. Additionally, more cracks are

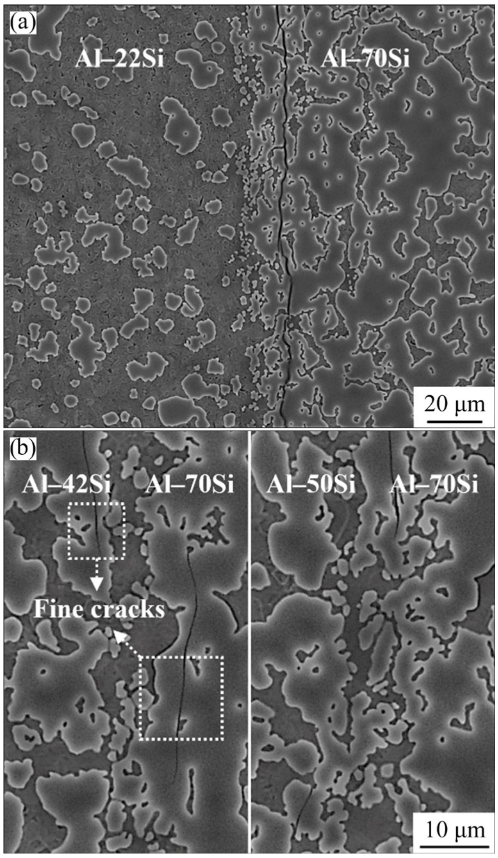

Fig. 10 SEM images of Al−22/70Si (a), and Al−42/70Si and Al−50/70Si (b) interfaces after thermal shock treatment

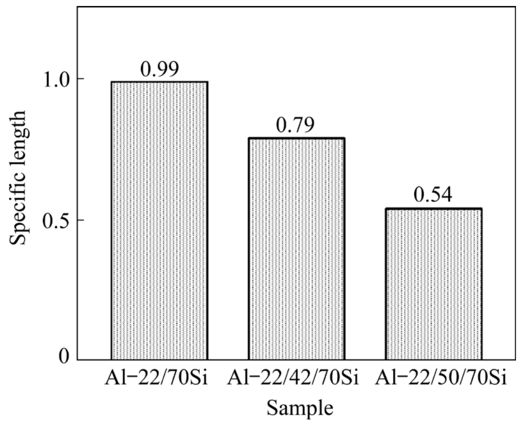

Fig. 11 Crack length per unit thickness in cross-section of Al−Si FGMs

observed in the two-layer FGM than in the three-layer FGMs, and near the 42/70 interface than near the 50/70 interface. Accordingly, the thermal shock resistance of the three FGMs can be evaluated.

To better understand the difference in thermal shock resistance among these samples, the axial stresses of the Al−Si FGMs from 25 to 300 °C are calculated using finite element analysis. The stress distribution in the central cross-section of the FGMs is shown in Fig. 12, and the axial stress as a function of thickness is shown in Fig. 13. During thermal shock treatment, stresses with different directions are generated at the interface of FGMs due to the CTE mismatch between the layers, resulting in a jump in stress when the thickness reaches the interface thickness. Therefore, cracks and broken Si phase are found near the interface. Compared with the three-layer FGMs, the two-layer FGM shows a larger jump and a higher thermal stress at the interface. This result explains the phenomenon that coarse cracks are observed in the two-layer FGM but not in the three-layer FGMs.

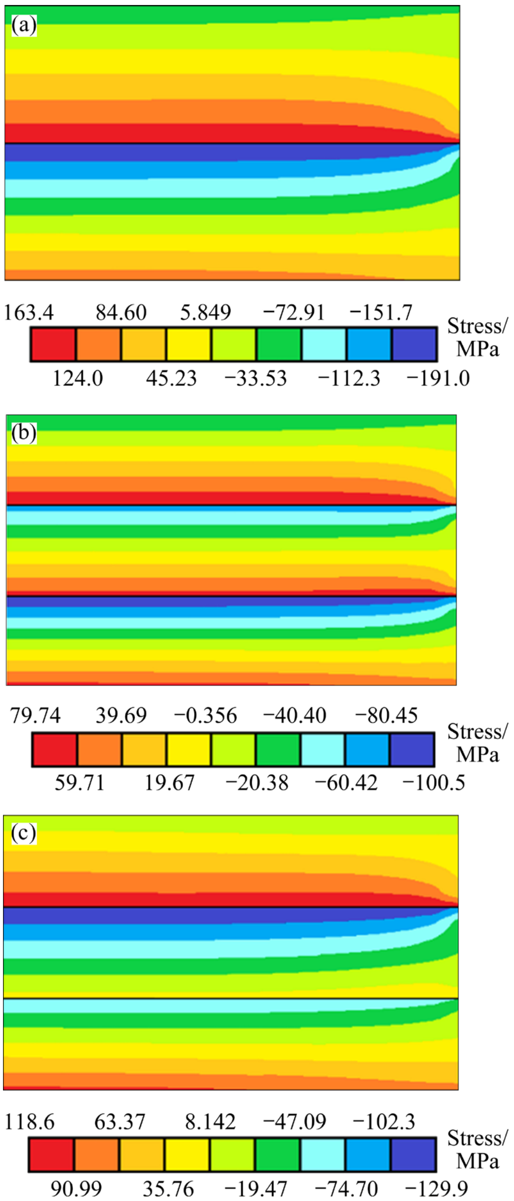

Fig. 12 Stress distribution in central cross-section of Al−22/70Si (a), Al−22/42/70Si (b), and Al−22/50/70Si (c) FGMs from 25 to 300 °C

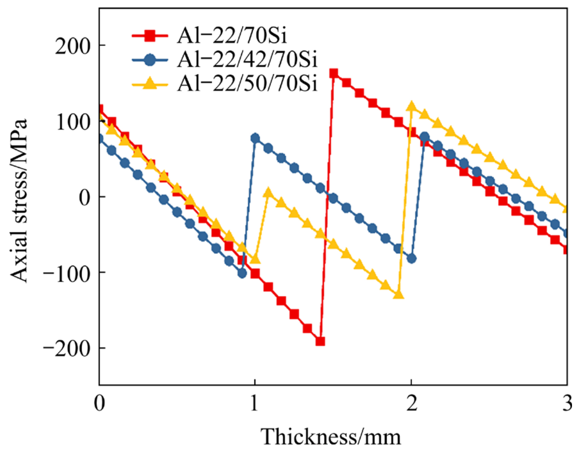

Fig. 13 Axial stress in central cross-section of Al−Si FGMs from 25 to 300 °C as function of thickness

Among the three-layer FGMs, the maximum thermal stress of the Al−22/50/70Si FGM is 119 MPa, higher than that of the Al−22/42/70Si FGM, which is 80 MPa. For the Al−22/42/70Si FGM, the maximum thermal stress occurs at the lower interface, while for the Al−22/50/70Si FGM it is the upper interface, which is consistent with the CTE mismatch between the layers. From this perspective, Al−42Si alloy seems to be a more suitable composition for the transition layer than Al−50Si alloy. However, more cracks are observed near the Al−42/70Si interface than near the Al−50/70Si interface. This phenomenon is due to the higher thermal stress of the Al−22/42/70Si FGM than the Al−22/50/70Si FGM, at the interface with high Si content that is prone to cracking, i.e., the Al−42/70Si and Al−50/70Si interfaces. The CTE mismatch of the lower interface plays a critical role here. As a result, the Al−22/50/70Si FGM exhibits better thermal shock resistance than the Al−22/42/70Si FGM. It can be concluded that increasing the number of layers, as well as selecting the appropriate transition layer composition, contributes to improving the thermal shock resistance of the Al–Si FGMs. However, more layers also imply more complicated fabrication processes and higher costs. Although increasing the number of layers seems to enhance the performance of the FGMs in all aspects, this needs to be taken into consideration.

4 Conclusions

(1) The two- and three-layer Al−Si FGMs with dense microstructure and good interlayer bonding are obtained by spray deposition. A smooth transition is observed at the interface of the FGMs, and the Si phase is uniformly distributed within each layer, with its morphology changing as the layer change.

(2) The Vickers hardness values at the interfaces are between those of the adjacent layers on both sides. The flexural strength of the three-layer FGMs is higher than that of the two-layer FGM, and the flexural strength in the H−L direction is higher than that in the L−H direction.

(3) The thermal conductivity and CTE of the constituent layers decrease as the Si content increases. The thermal conductivity of all the FGMs exceeds 140 W/(m·K), while the CTE shows no significant difference. Compared with the two-layer FGM, the three-layer FGMs significantly improve CTE matching while maintaining high thermal conductivity.

(4) After thermal shock treatment, more cracks are found in the two-layer FGM than in the three-layer FGMs, and near the 42/70 interface than near the 50/70 interface. This phenomenon is due to the high thermal stresses at the interfaces and the tendency of large Si particles to rupture as a result of stress concentration.

Acknowledgments

The authors are grateful for the financial support provided by the National Natural Science Foundation of China (No. 52274369), the China Postdoctoral Science Foundation (No. 2018M632986), the Natural Science Foundation of Hunan Province, China (No. 2019JJ50766), the Postdoctoral Science Foundation of Central South University, China, and the Science and Technology Program of Hunan, China (No. 2020GK2044).

References

[1] TONG X C. Advanced materials for thermal management of electronic packaging [M]. New York: Springer, 2011.

[2] DONG Cui-ge, WANG Ri-chu, CHEN Yi-xin, WANG Xiao-feng, PENG Chao-qun, ZENG Jing. Near-net shaped Al/SiCP composites via vacuum-pressure infiltration combined with gelcasting [J]. Transactions of Nonferrous Metals Society of China, 2020, 30(6): 1452−1462.

[3] HONG Yu, WANG Wu-jie, LIU Jia-qin, TANG Wen-ming, WU Yu-cheng. Effect of porosity and interface structures on thermal and mechanical properties of SiC_p/6061Al composites with high volume fraction of SiC [J]. Transactions of Nonferrous Metals Society of China, 2019, 29(5): 941−949.

[4] FAN Rui, HUANG Ying, HAN Xiao-ping, PENG Xuan-yi. High thermal conductivity and mechanical properties of Si@graphite/aluminum nitride/aluminum composites for high-efficiency thermal management [J]. Journal of Alloys and Compounds, 2021, 858: 157630.

[5] WEI Xin, CHEN Guo-dong, WANG Bing, CHEN Guo-hong, YANG Lei, TANG Wen-ming. Characteristics and grinding performance evaluation of the high-fraction GNFs/SiC_p/6061Al matrix hybrid composites [J]. Journal of Alloys and Compounds, 2021, 867: 159049.

[6] CAI Zhi-yong, ZHANG Chun, WANG Ri-chu, PENG Chao-qun, WU Xiang, LI Hai-pu. High-temperature mechanical properties and thermal cycling stability of Al−50Si alloy for electronic packaging [J]. Materials Science and Engineering A, 2018, 728: 95−101.

[7] LIU Jun-wu, JIANG Dao-chuan, ZHOU Xing-xing, WANG Yong-hong, LIU Xue-min, XIN Hong-xing, JIANG Yang, YANG Lei, ZHANG Yu-jun, HUANG Zhi-gang, FENG Dong. Microstructure and properties of Al−60wt.%Si composites prepared by powder semi-solid squeeze [J]. Powder Technology, 2019, 343: 95−100.

[8] LIU Yan-qiang, FAN Jian-zhong, HAO Xin-xiang, WEI Shao-hua, NIE Jun-hui, MA Zi-li, LIU Ming-kun, WANG Ya-bao. Advanced hermetic electronic packaging based on lightweight silicon/aluminum composite produced by powder metallurgy technique [J]. Rare Metals, 2020, 39(11): 1307−1313.

[9] CAI Zhi-yong, ZHANG Chun, WANG Ri-chu, PENG Chao-qun, WU Xiang, LI Hai-pu, YANG Ming. Improvement of deformation capacity of gas-atomized hypereutectic Al−Si alloy powder by annealing treatment [J]. Transactions of Nonferrous Metals Society of China, 2018, 28(8): 1475−1483.

[10] DAI H S, LIU X F. Refinement performance and mechanism of an Al−50Si alloy [J]. Materials Characterization, 2008, 59(11): 1559−1563.

[11] FANG Jun, ZHONG Yong-hui, XIA Ming-kuang, ZHANG Feng-wei. Mechanical and thermo-physical properties of rapidly solidified Al−50Si−Cu(Mg) alloys for thermal management application[J]. Transactions of Nonferrous Metals Society of China, 2021, 31(3): 586−594.

[12] WANG Feng, XIONG Bai-qing, ZHANG Yong-an, ZHU Bao-hong, LIU Hong-wei WEI Yan-guang. Microstructure, thermo-physical and mechanical properties of spray-deposited Si−30Al alloy for electronic packaging application [J]. Materials Characterization, 2008, 59(10): 1455−1457.

[13] LI Yan-xia, LIU Jun-you, WANG Wen-shao, LIU Guo-quan. Microstructures and properties of Al−45%Si alloy prepared by liquid–solid separation process and spray deposition [J]. Transactions of Nonferrous Metals Society of China, 2013, 23(4): 970−976.

[14] XIU Zi-yang, CHEN Guo-qin, WANG Xiao-feng, WU Gao-hui, LIU Yan-mei, YANG Wen-shu. Microstructure and performance of Al−Si alloy with high Si content by high temperature diffusion treatment [J]. Transactions of Nonferrous Metals Society of China, 2010, 20(11): 2134−2138.

[15] KANG Nan, CODDET P, AMMAR M R, LIAO Han-lin, CODDET C. Characterization of the microstructure of a selective laser melting processed Al−50Si alloy: Effect of heat treatments [J]. Materials Characterization, 2017, 130: 243−249.

[16] CUI C, SCHULZ A, SCHIMANSKI K, ZOCH H-W. Spray forming of hypereutectic Al−Si alloys [J]. Journal of Materials Processing Technology, 2009, 209(11): 5220−5228.

[17] JIA Yan-dong, CAO Fu-yang, SCUDINO S, MA Pan, LI Hai-chao, YU Lei, ECKERT J, SUN Jian-fei. Microstructure and thermal expansion behavior of spray-deposited Al−50Si [J]. Materials & Design, 2014, 57: 585−591.

[18] HAQUE A, SHEKHAR S, NARAYANA MURTY S V S, RAMKUMAR J, KAR K, MONDAL K. Fabrication of controlled expansion Al−Si composites by pressureless and spark plasma sintering [J]. Advanced Powder Technology, 2018, 29(12): 3427−3439.

[19] SARASWAT E, MAHARANA H S, NARAYANA MURTY S V S, SHEKHAR S, KAR K K, RAMKUMAR J, MONDAL K. Fabrication of Al−Si controlled expansion alloys by unique combination of pressureless sintering and hot forging [J]. Advanced Powder Technology, 2020, 31(7): 2820−2832.

[20] ZHANG Yong-yun, FENG Shi-hui, DING Chao, NODOOSHAN H R J, YE Shu-long, JIANG Feng, LI Zhong, GU Meng, YU Peng. Investigation of the influences of heat treatment on the microstructures and thermal properties of Al−20Si alloy fabricated by powder extrusion [J]. Materials Characterization, 2020, 168: 110522.

[21] YU Kun, LI Shao-jun, CHEN Li-san, ZHAO Wei-shang, LI Peng-fei. Microstructure characterization and thermal properties of hypereutectic Si−Al alloy for electronic packaging applications [J]. Transactions of Nonferrous Metals Society of China, 2012, 22(6): 1412−1417.

[22] LIU Hong-wei, HUANG Shu-hui, LI Zhi-hui, XIONG Bai-qing, ZHANG Yong-an, LI Xi-wu, YAN Hong-wei, YAN Li-zhen. Microstructure and properties of spray-formed Si−30Al alloy used for electronic packaging [C]//High Performance Structural Materials. Singapore: Springer, 2018: 79−86.

[23] PANDEY P M, RATHEE S, SRIVASTAVA M, JAIN P K. Functionally graded materials (FGMs): Fabrication, properties, applications, and advancements [M]. Boca Raton: CRC Press, 2021.

[24] SALEH B, JIANG Jing-hua, FATHI R, AL-HABABI T, XU Qiong, WANG Li-sha, SONG Dan, MA Ai-bin. 30 Years of functionally graded materials: An overview of manufacturing methods, applications and future challenges [J]. Composites Part B: Engineering, 2020, 201: 108376.

[25] ZHOU Hong-yu, LIU Xin, YIN Zheng, LI Ya-qiang, LIU Chang, LIU Shi-bin, WU Chun-jing, LIU Jun-you. The fabrication of functional gradient hypereutectic Al-Si composites by liquid-solid separation technology [J]. Journal of Alloys and Compounds, 2018, 763: 49−55.

[26] HUO Shao-xin, CHEN Qi-hai, ZHOU Ying-qiao, XING Da-wei, WANG Bin. The preliminary study of gradient AlSi alloy fabricated by 3D printing technology [C]//2021 IEEE International Conference on Electrical Engineering and Mechatronics Technology (ICEEMT). Qingdao: IEEE, 2021: 179−183.

[27] SHACKELFORD J F, HAN Y H, KIM S, KWON S-H. CRC materials science and engineering handbook [M]. CRC Press, 2016.

[28] ZWEBEN C. Metal-matrix composites for electronic packaging [J]. JOM, 1992, 44(7): 15−24.

[29] DAVIS L C, ARTZ B E. Thermal conductivity of metal-matrix composites [J]. Journal of Applied Physics, 1995, 77(10): 4954−4960.

[30] BHATTACHARYYA M, KUMAR A N, KAPURIA S. Synthesis and characterization of Al/SiC and Ni/Al_2O_3 functionally graded materials [J]. Materials Science and Engineering A, 2008, 487(1): 524−535.

[31] ZHANG Wen-long, DING Dong-yan, GAO Ping. High volume fraction Si particle-reinforced aluminium matrix composites fabricated by a filtration squeeze casting route [J]. Materials & Design, 2016, 90: 834−838.

[32] ZUO Kai-hui, JIANG Dong-liang, LIN Qing-ling. Mechanical properties of Al_2O_3/Ni laminated composites [J]. Materials Letters, 2006, 60(9/10): 1265−1268.

[33] WU Chuan-dong, WU Jia-lu, MA Ka-ka, ZHANG Da-long, XIONG Shu-ya, ZHANG Jian, LUO Guo-qiang, CHEN Fei, SHEN Qiang, ZHANG Lian-ming, LAVERNIA E J. Synthesis of AA7075−AA7075/B_4C bilayer composite with enhanced mechanical strength via plasma activated sintering [J]. Journal of Alloys and Compounds, 2017, 701: 416−424.

[34] GAO Shuai, NAN Zong-liang, LI Yi, ZHAO Nan, LIU Qin-qin, XU Gui-fang, CHENG Xiao-nong, YANG Juan. Copper matrix thermal conductive composites with low thermal expansion for electronic packaging [J]. Ceramics International, 2020, 46(11): 18019−18025.

[35] CAI Zhi-yong, WANG Ri-chu, ZHANG Chun, PENG Chao-qun, FENG Yan, WANG Lin-qian. Thermal cycling reliability of Al/50Si_p composite for thermal management in electronic packaging [J]. Journal of Materials Science: Materials in Electronics, 2015, 26(7): 4894−4901.

电子封装用 Al−Si 功能梯度材料的显微组织和性能

周 玮[1]，王日初[1,2]，彭超群[1]，蔡志勇[1,2]

1. 中南大学 材料科学与工程学院，长沙 410083；
2. 中南大学 电子封装与先进功能材料重点实验室，长沙 410083

摘　要：通过喷雾沉积法制备用于电子封装的双层和三层 Al−Si 功能梯度材料。结果表明，梯度材料具有致密的显微组织和良好的层间结合。三层梯度材料的抗弯强度高于双层梯度材料，以高 Si 含量层为承载面的 H−L 方向的抗弯强度高于以低 Si 含量层为承载面的 L−H 方向。所有梯度材料的导热系数均超过 140 W/(m·K)，且其热膨胀系数没有明显的差异。经热冲击处理后，双层梯度材料出现的裂纹比三层梯度材料更多更大，这是由于界面上的高热应力和大尺寸 Si 颗粒因应力集中而趋于破裂。

关键词：电子封装；功能梯度材料；Al−Si 合金；有限元分析；抗热震性能

(Edited by Xiang-qun LI)